Journal of Biomechanics 162 (2024) 111914

Contents lists available at ScienceDirect

Journal of Biomechanics

journal homepage: www.elsevier.com/locate/jbiomech

Can wall shear-stress topology predict proliferative vitreoretinopathy localization following pars plana vitrectomy?

P.G. Ledda [a], T. Rossi [b], M.G. Badas [a], G. Querzoli [a,*]

[a] DICAAR, Università degli Studi di Cagliari, Cagliari, Italy
[b] IRCCS Fondazione G.B. Bietti ONLUS, Rome, Italy

ARTICLE INFO

Keywords:
Retina
Proliferative vitreoretinopathy
Fluid dynamics
Wall shear stresses
Manifold theory

ABSTRACT

We numerically study the fluid dynamics of oil tamponade in models of vitrectomized eyes prompted by a subset of daily activities corresponding to movements on the horizontal plane with the patient in a standing position. Bulk flow features are related to near-wall flow topology and transport at the retinal surface through a wall shear-stress-based analysis. Proliferative VitreoRetinopathy (PVR) is the leading cause of retinal re-detachment occurring in about 20% of all cases due to the accumulation of inflammatory cells in discrete retinal regions. Signalling soluble mediators stimulate inflammatory cells' chemotaxis and studying their distribution across the retinal surface may acquire clinical relevance. In all the investigated cases, persistent and elongated regions along the retina, potentially prone to accumulate chemo-attractants and cells are observed. Gradients of soluble inflammation mediators present in the aqueous are known responsible for the so-called epithelial-mesenchymal transition that initiates PVR and favours recurrent retinal detachment prompting the proliferation of inflammatory cells with collagen matrix deposition and its contraction. The surgical apposition of encircling scleral buckling elements, known for over a century to influence PVR formation and localization, modifies the attracting regions, possibly causing an accumulation of molecules and cells along approximately vertical lines that follow the rising menisci due to the cerclage indentation. The resulting spatial pattern is compatible with clinical observations. This study may open toward rational analyses of near-wall transport to predict PVR pathogenesis by relating biochemical accumulation in certain areas of the retina to clinical conditions.

1. Introduction

The pars plana vitrectomy is a surgical procedure performed to repair complex retinal detachments and consists in the replacement of the vitreous with a fluid substitute (*tamponade*), which coexists with an unavoidable fraction of aqueous continuously produced by the eye (Ando et al., 1986; Bonnet et al., 1987; Kleinberg et al., 2011; Romano et al., 2021). The presence of the tamponade reduces aqueous contact with retinal tears, thus reducing the risk of re-detachment but changes the fluid dynamics within the vitreous chamber. The high viscosity (ranging from 1 to 5 Pa s) of the silicone oil (SO) corresponds to high wall shear-stresses (WSS), while the immiscibility with water alters the near-wall transport of chemical substances and cells. Though after surgery patients are instructed to maintain prescribed postures to keep the region of the retinal tear(s) in contact with SO (Hostovsky et al., 2020), tamponade motion within the vitreous chamber due to everyday activities is unavoidable and may affect recovery. Whilst gas tamponade exhibits sloshing movements (Angunawela et al., 2011; Rossi et al., 2023), SO tamponade is less prone, also because of the slight weight difference with the aqueous (Fawcett et al., 1994). Nevertheless, much larger forces developing at the retinal surface, compared to the gas-tamponade case, have been observed following saccadic movements (Rossi et al., 2022). The dynamics of SO consequent to everyday movements is worth a detailed investigation since the distribution and intensity of wall shear-stresses play a key role in the near-wall transport processes, which in turn may promote retinal re-detachment (Angunawela et al., 2011). Several works investigated SO tamponade in static conditions, in spherical (Fawcett et al., 1994) and in realistic geometries (Isakova et al., 2017). These authors showed a sensitivity of the interface to geometrical eye changes, as confirmed by Rossi et al. (2021, 2022). The anterior region of the vitreous chamber is deformed by the indentation of the lens that induces two rising menisci on its sides because of the small curvature radius. Also other conditions, such as high myopia, staphyloma or *scleral buckling*, SB, (the insertion of an encircling band to

* Corresponding author at: Dipartimento di Ingegneria Civile, Ambientale e Architettura, Università degli Studi di Cagliari, Via Marengo 2, 09123 Cagliari, Italy.
E-mail address: querzoli@unica.it (G. Querzoli).

https://doi.org/10.1016/j.jbiomech.2023.111914
Accepted 20 December 2023
Available online 27 December 2023

promote retinal re-attachment), alter the vitreous chamber geometry and modify the static configuration, with the aqueous meniscus that rises in the highly concave regions and descends where the surface is convex (Rossi et al., 2022). Saccadic movements (i.e. the sudden eye rotations to gaze at an object) with SO tamponade have been the testing ground for several investigations, often focused on assessing the role of the WSS distribution in retinal stretch (Rossi et al., 2021, 2022) and SO emulsification (De Silva, 2005; Wang et al., 2021).

In this context, soluble molecules from retinal tears within the vitreous chamber may induce pathology. Proliferative vitreoretinopathy (PVR) is a complex inflammatory process representing the main cause of recurrent retinal detachment which starts with the recruitment and proliferation of inflammatory cells, the transition of epithelial cells into mesenchymal progenitors capable of secreting collagen and the contraction of such material deposited over the surface and within the retinal layers (Lewis et al., 2002). PVR finds its pathogenesis in the migration of retinal pigment epithelium and glial cells from retinal breaks, transported by the flow inside the vitreous chamber (Chaudhary et al., 2020). Often, it develops in the inferior region, where SO is not in contact with the retina in standing conditions (Barbosa et al., 2022). These cells accumulate in specific regions of the surface, induce inflammation, and proliferate. The consequence is an increase in retinal traction that may lead to a re-detachment (see e.g. Chaudhary et al., 2020 for a detailed picture).

In the case of inferior detachment, the apposition of encircling elements (scleral buckles and encircling bands) counteracts the retinal stiffness induced by PVR (Wei et al., 2016). In Fig. 1(a), we report an anonymized retinography of a post-vitrectomy eye, treated with an encircling band. The picture depicts the initial stage of PVR, with a well-distinguished meridional fold with retinal stiffening (the whitish region highlighted by the dashed rectangle) that develops close to the scleral buckling element. Fig. 1(b) instead shows the late-stage of PVR, with the formation of wrinkles over the retinal surface that interest the full thickness of the retina, the so-called starfolds (red rectangles).

The identification of persistent patterns can be related to clinical conditions to assess the possible pathogenesis of PVR, in sensitive regions. Therefore, understanding the near-wall flow patterns for different eye geometries may point out retinal regions more prone to the accumulation of soluble molecules stimulating chemotaxis and the development of PVR and hopefully offer solutions to prevent it. Here, we investigate the fluid dynamics of silicone oil tamponade, at different filling fractions, driven by a subset of everyday movements in the horizontal plane, for a standing patient. We rationalize the role of the bulk flow features in near-wall biochemical transport and assess the effect of idealized geometry modifications induced by a staphyloma and a cerclage.

In Section 2, we present steady solutions at various filling percentages that constitute the initial conditions for the fluid dynamics of Section 3. Section 4 investigates the near-wall patterns and their relationship with biochemical transport and the possible development of PVR.

2. Problem formulation and numerical approach

We numerically study the multiphase flow of silicone oil tamponade with aqueous at different filling fractions in a model of a human vitreous chamber. The physical properties of aqueous (density $\rho = 997$ kg/m^3, viscosity $\mu = 10^{-3}$ Pa s) and SO ($\rho = 970$ kg/m^3, $\mu = 1$ Pa s), as well as their surface tension coefficient $\gamma = 44$·mN/m and contact angle (16.2° between aqueous and retinal walls (Rossi et al. 2022)), ensure realistic fluid dynamics, wetting and interfacial properties. The investigated eye geometries are shown in Fig. 2. We consider (a) a healthy model (*emmetropic*), formed by a sphere of radius $R = 12$ mm, with its anterior part flattened to mimic the presence of the lens in an aphakic eye (Rossi et al., 2022). The emmetropic eye is compared against (b) a pathologic condition with the presence of a posterior staphyloma and (c) the case of encircling band insertion. We consider three different movements from Rossi et al. (2023), all occurring in the horizontal plane (Fig. 2d,e,f). The first one is (d) a saccade, based on a polynomial law with a 50° amplitude and a 0.1375 s duration, and a peak angular velocity of 546.67°/s (Stocchino et al., 2010). Subsequently, we consider an ideal sudden car braking, from approx. 20 km/hour to the complete stop, with a linear increase of deceleration from 0 to 0.5 g in 0.1 s, then kept constant for 1 s, and followed by a linear decrease to zero in 0.1 s (mimicking the increasing pressure of the brake pedal, the constant pressure phase, and the final pedal release). These two movements are examples of angular and linear accelerations occurring in the real life. The third movement is a head rotation (f) i.e. a combination of linear and angular accelerations, obtained by image-analysis of a high-speed video-recording of a volunteer asked to turn the head to the left and then return to the original position (Rossi et al., 2023). The analysis investigates the motion and the following instants with the eye at rest (*relaxation phase*).

The two immiscible fluids are simulated through the Volume-of-Fluid (VOF) method embedded in the finite-volume solver OpenFOAM (Weller et al., 1998), which couples the Navier-Stokes equations, solved in the frame of the eye, with the transport of the water volume fraction α within the chamber volume V enclosed by the surface S. We refer to the Supplementary Material for further insight into numerical

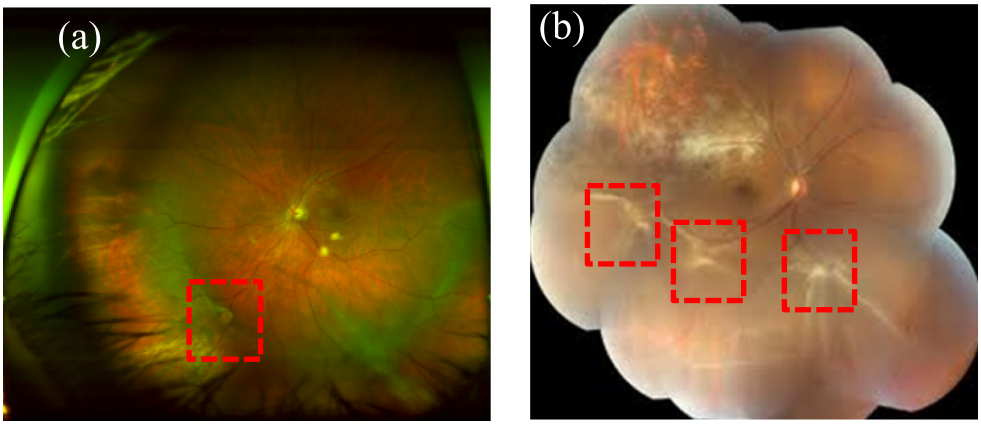

Fig. 1. Retinographs from anonymized patients who developed PVR after vitrectomy. (a) Initial stage of retinal contraction (PVR), highlighted by the presence of a meridional retinal fold within the red box. (b) Late-stage PVR: areas of proliferation of mesenchymal and inflammatory cells are the so-called starfolds (e.g. red boxes), where cells accumulate transported by near-surface flows, proliferate and grow over the retinal surface and within the retinal layers, locally increasing the rigidity and eventually leading to retinal re-detachment. (For interpretation of the references to colour in this figure legend, the reader is referred to the web version of this article.)

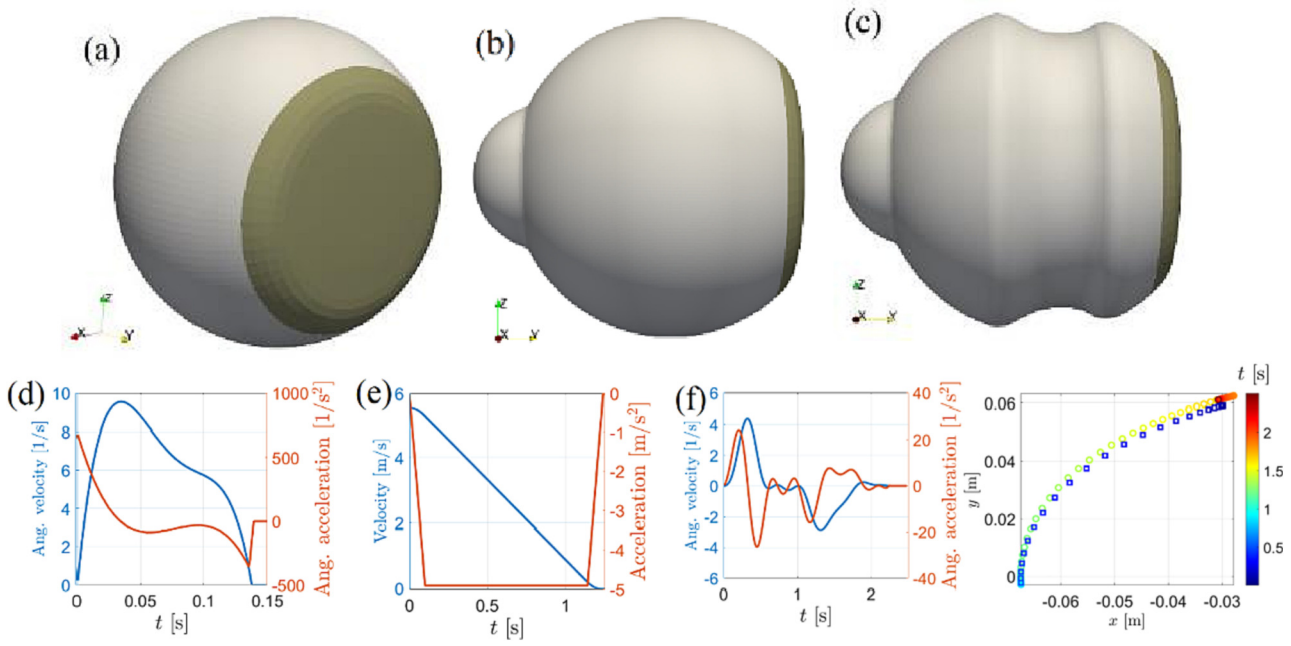

Fig. 2. (a,b,c) Considered models of the human eye: (a) emmetropic eye, (b) posterior staphyloma and (c) encircling band. The retinal surface is coloured white. (d,e, f) Movements considered in this work:, (d) saccade, (e) linear deceleration, (f) head rotation around the origin. Left panel of (f) shows the trajectory with time of the eye centre of mass; filled dots are employed for the first phase of the movement, whilst empty ones for the second phase.

implementation and grid convergence analysis, based on previously published works (Rossi et al., 2021,2022).

3. Static interface: Retinal surface wetting

The initial condition is the equilibrium between the aqueous and SO resulting from the balance between surface tension and gravity (which points downwards in Fig. 2), with an imposed contact angle at the solid surfaces. The Bond number, $Bo = \Delta\rho g R^2/\gamma$, which measures the ratio of gravity to surface tension, is of the order of the unity, with the density difference between the two fluids being $\Delta\rho = 17$ kg/m^3. Therefore, the interface shape is mainly driven by surface tension, resulting nearly spherical with a large meniscus induced by SO hydrophobicity (Fig. 3). An increase in the SO fraction leads to the progressive downward displacement of the contact line and to the increase of the retinal surface fraction in contact with the tamponade (Fig. 3b,c). A large surface contact with SO is obtained only when almost all the volume is filled with SO, whereas the lowest part of the retina is never in contact with SO due to buoyancy.

Modifications in the eye geometry induce meaningful variations of the interface shape (Fig. 3d,e,f). The presence of a staphyloma alters the inclination of the interface at high filling fractions, with the tamponade confined below the bulge. Conversely, encirclement bands modify the interface shape, with two rising water layers near the indentation and the consequent thinning of the bulk aqueous region, resulting in decreasing the upper retinal surface in contact with SO. These features will have consequences on the fluid dynamics, as shown next.

4. Fluid dynamics following everyday activities

Fig. 4(a,c,e) shows the time evolution of the average velocity:

$$< u >= \frac{1}{V}\int_V |\boldsymbol{u}| dV.$$

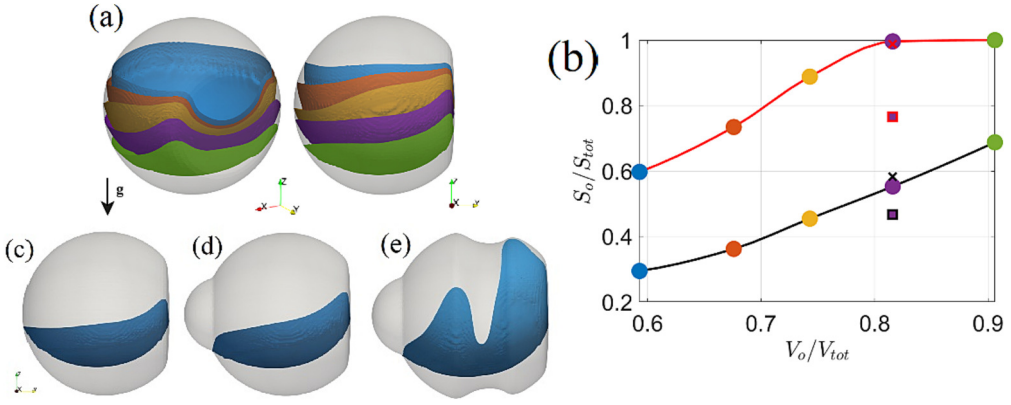

Fig. 3. (a) Interface of an emmetropic eye for the different filling fractions reported in the plot of panel (b), which shows the fraction of total (black) and superior (red) retinal surface S_o (white region in Fig. 1) in contact with tamponade as a function of the filling (i.e. the ratio of the silicone oil volume V_o to the total volume V) for the emmetropic eye (circles), posterior staphyloma (crosses) and encirclement band (squares) case. (c,d,e) Interface position for the 82% filling: (c) emmetropic eye, (d) posterior staphyloma, (e) encircling band. (For interpretation of the references to colour in this figure legend, the reader is referred to the web version of this article.)

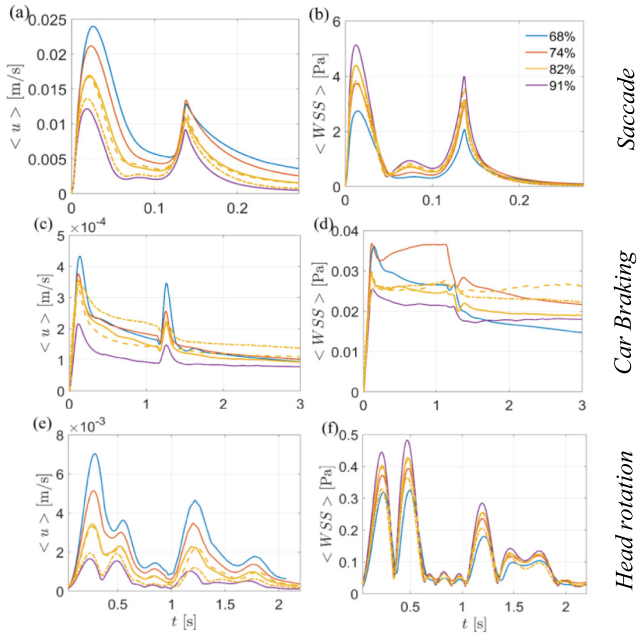

Fig. 4. Variation of the average velocity, $\langle u \rangle$ (a,c,e) and surface-averaged WSS (b,d,f) as functions of time, for: (a,b) saccade, (c,d) car braking, (e,f) head rotation. Solid, dashed and dash-dotted lines correspond to the emmetropic, staphyloma and SB cases, respectively. Colours correspond to a different SO filling for the emmetropic case.

Irrespective of the movement, there are two peaks at the initial and final instants of the motion, when accelerations are higher. In the head rotation case, the intermediate peaks are induced by the return phase after the complete side rotation. The time-histories of the surface-averaged magnitude of wall shear-stresses $< WSS > = \frac{1}{S}\int_S |\boldsymbol{\tau}| dS$.

well follow those of average velocity (Fig. 4(b,d,f)). The different orders of magnitude of $<WSS>$ are in agreement with the corresponding motion acceleration and average velocity magnitude (Fig. 4(a,c,e)). Therefore, saccade leads to much higher $<WSS>$ values compared to the other two movements, while head rotation determines higher $<WSS>$ than car braking.

The peak value of $<u>$ is nearly halved in the case of saccade and braking, while it is reduced to one-third in the case of head rotation, when the filling fraction increases by one-third, indicating that the energy is not transmitted to SO proportionally to its mass. The peak value of the surface-averaged WSS decreases with SO filling fraction. The time evolutions for different fillings, in the emmetropic case, appear remarkably similar (see continuous lines of different colours), suggesting that overall fluid dynamic features do not change dramatically. We thus focus the discussion on the 82% SO filling. The staphyloma case (orange dashed lines) does not present significant deviations from the emmetropic case, whilst encircling bands (orange dot-dashed lines) have a greater influence on the considered average quantities.

During the investigated movements, the SO-aqueous interface exhibits only extremely small motions and therefore they are not shown nor discussed here.

We now describe the spatial structure of the flow. Fig. 5 shows the velocity field (relative to the frame of the eye), at the beginning of the saccade ($t_1 = 0.05$ s) and relaxation ($t_2 = 0.15$ s) phases. The angular acceleration induces a recirculating motion in both fluids. The largest velocities are localized in the aqueous, just below the meatus generated by the hydrophobic contact angle. A posterior staphyloma (second row of Fig. 5) induces slightly larger maximum velocities, attained more uniformly and closer to the rotation centre, compared to the emmetropic case. The cerclage case (third row of Fig. 5) presents weaker velocities and a more intricate structure due to the rising of water on the side of the

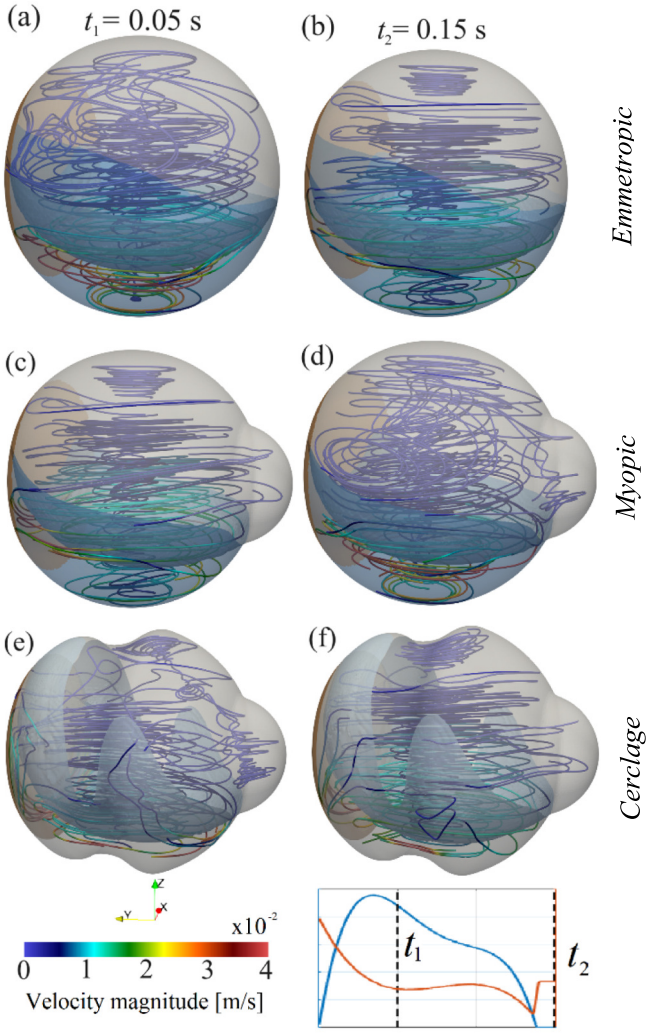

Fig. 5. Streamlines of the relative velocity field in the case of emmetropic eye with 82% filling for a saccadic movement: left column (a,c,e) at $t_1 = 0.05$ s during the rotation; right column (b,d,f) at $t_2 = 0.15$ s during the relaxation phase: first row (a,b) emmetropic eye, second row (c,d) staphyloma, third row (e,f) cerclage. In the lower panel of subfigure (f), velocity and acceleration are shown as a function of time with the instants t_1 and t_2 indicated with dashed lines.

vitreous chamber, at very large heights. The flow appears to be the superposition of an overall rotating motion with two recirculations developing in the regions separated by the indentation, with non-negligible vertical components in the uprising portions of the interface.

Fig. 6 shows the fluid dynamics features in the car braking case of Fig. 1(e). The relative velocity field presents an overall recirculation around the horizontal axis orthogonal to the deceleration direction, with the largest values localized in the aqueous, where a ring-shaped region of large velocity is identified. These features persist during acceleration and relaxation. However, smaller velocities are generally observed, compared to the saccade.

The staphyloma does not change the scenario. Conversely, an encircling band breaks the previously observed ring-shaped region, with large velocities in the rising menisci and at the indentation. The fluid dynamics associated with the head rotation (Fig. 7) shows similarities with the saccadic case, for all geometries.

In summary, a posterior staphyloma does not significantly alter the structure of the flow observed in the emmetropic eye, although with slightly larger velocities in the aqueous. Conversely, an encircling band induces a more confined flow in the aqueous, due to the intricate

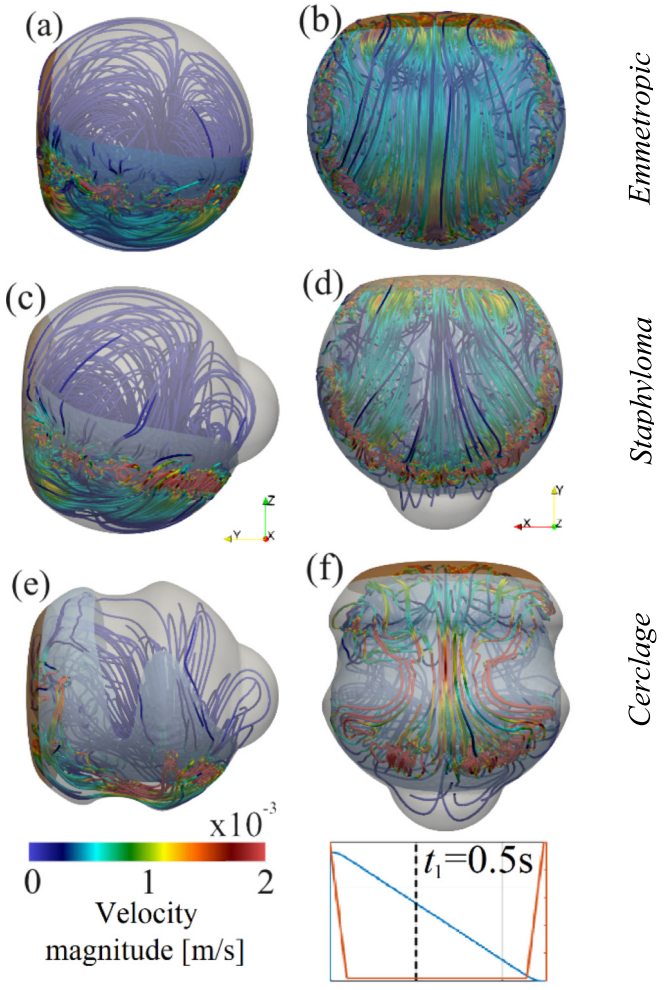

Fig. 6. Streamlines of the relative velocity field at $t_1 = 0.5$ s for the idealized car braking with 82% filling: (a,b) emmetropic eye, (c,d) posterior staphyloma and (e,f) scleral buckling. In the lower panel of subfigure (f), velocity and acceleration are shown as a function of time with the instant t_1 indicated with a dashed line.

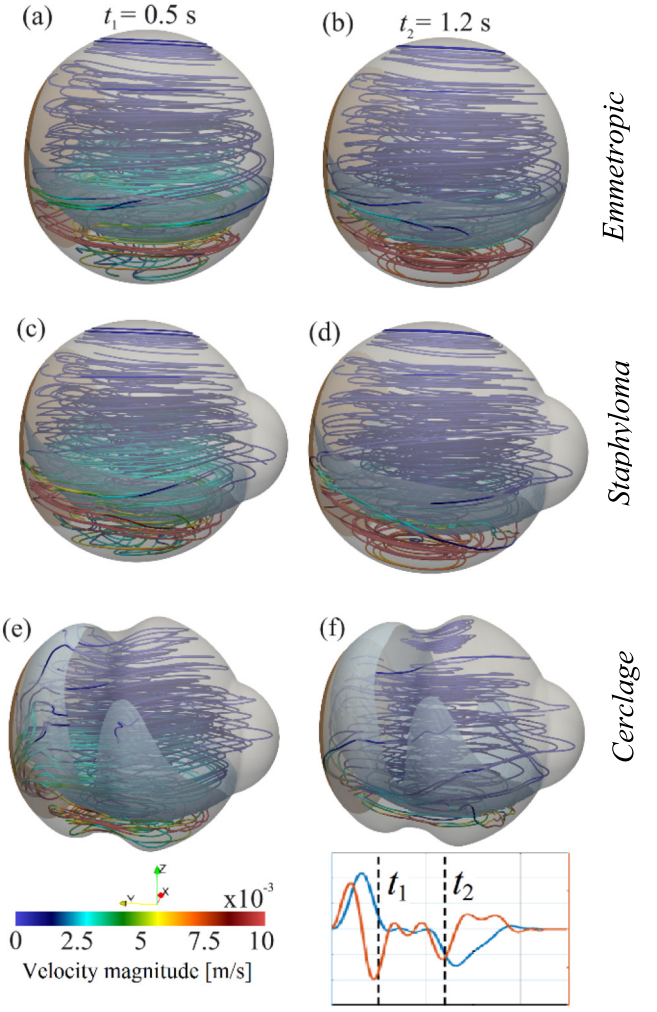

Fig. 7. Streamlines of the relative velocity field during head rotation at (a,c,e) $t_1 = 0.5$ s and (b,d,f) $t_2 = 1.2$ s, with 82% filling. (a,b) Emmetropic eye; (c,d) Staphyloma case; (e,f) Scleral buckling case. In the lower panel of subfigure (f), velocity and acceleration are shown as a function of time with the instants t_1 and t_2 indicated with dashed lines.

interface that makes the aqueous domain thinner. An increase in the SO filling progressively reduces the flow kinetic energy and dissipation. Henceforth, these fluid-dynamics features are translated into quantities of interest at the retinal walls through maps of the WSS and rationalized via their manifold properties. Eventually, the potential clinical consequences related to these fluid dynamics indexes are discussed.

5. From bulk flow to manifold characterization: Wall shear-stress topology

Wall shear-stresses have a twofold physical meaning in the present context. They represent the solicitations exerted on the retina, possibly promoting its displacement and re-detachment after the surgery; also, the velocity in the proximity of the walls is aligned with the WSS vector $\boldsymbol{\tau}$, i.e. $\boldsymbol{u} \propto \boldsymbol{\tau}$, in a first-order approximation (Gambaruto and João, 2012). Coherent structures in the WSS vector thus depict salient features of the near-wall velocity field and transport (Arzani et al., 2016, 2017; Arzani and Shadden, 2016, 2018). Within an Eulerian framework (Mazzi et al., 2020, 2021), we gain insight into the average near-wall flow topology (i.e. streamlines distribution) by analysing the divergence of the time-averaged ($\bar{\cdot}$) normalized wall shear-stress vector $\mathrm{DIV}_{\mathrm{WSS}} = \nabla \cdot \left(\frac{\bar{\boldsymbol{\tau}}}{|\bar{\boldsymbol{\tau}}|} \right)$ (De Nisco et al., 2020; Morbiducci et al., 2020; Mazzi et al., 2021; Ledda et al., 2023). Regions of large negative divergence are called attracting manifolds since they depict converging streamlines of the time-averaged WSS and velocity and the consequent accumulation of biochemicals flowing along the surface, whereas positive $\mathrm{DIV}_{\mathrm{WSS}}$ regions indicate that the near-wall transport promotes low concentrations of biochemicals (repelling manifolds). The attracting manifolds typically converge in particular (*critical*) points of the field, i.e. stable nodes and focuses, where intense accumulation occurs (Mazzi et al., 2021).

It is reasonable to presume that soluble molecules present in the aqueous because of blood-retinal barrier breakdown, invariably present in rhegmatogenous retinal detachment, tend to accumulate in negative $\mathrm{DIV}_{\mathrm{WSS}}$ regions (attracting manifolds), with the consequent creation of gradients (as opposed to a well-mixed condition of soluble molecules and cells). These gradients can start inflammation cells chemotaxis, initiating the inflammatory cascade where molecules accumulate, especially if those attracting manifolds happen to exist in the nearby of retinal vessels from where most inflammatory cells derive.

Also, the above-defined manifolds depict preferential directions of retinal traction (with possible re-detachment along these lines if abnormally high shear-stresses are also observed), which may act in positive feedback with cell transport. Fig. 8 presents the time-averaged wall shear-stress magnitude ($\overline{\mathrm{WSS}}$) and $\mathrm{DIV}_{\mathrm{WSS}}$ during the whole simulated saccadic movement and relaxation. From a quantitative point of

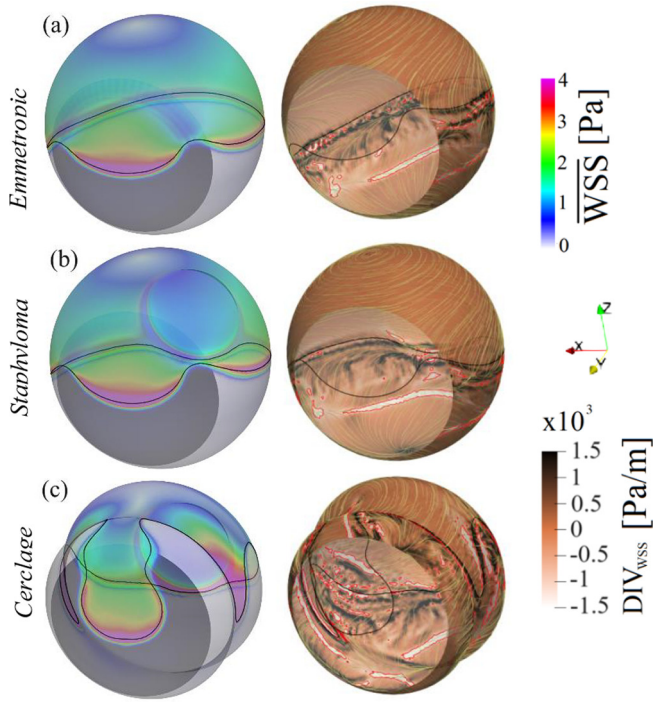

Fig. 8. Saccadic motion for 82% filling. Colormaps of time-averaged (left) WSS and (right) DIV_{WSS} in the (a) emmetropic, (b) staphyloma and (c) scleral buckling cases. While the left panel is slightly transparent to observe the whole WSS patterns, with the pars plana highlighted in grey, the right panels do not present the pars plana region and streamlines (yellow lines) help in identifying the attracting manifolds (which present negative divergence values and converging streamlines). The red-contoured, white regions denote the attracting manifolds, defined by the threshold value $DIV_{WSS} = 1000$ Pa/m. (For interpretation of the references to colour in this figure legend, the reader is referred to the web version of this article.)

view, we identify the most intense attracting manifolds through the threshold $DIV_{WSS} = -1000$ Pa/m, which roughly corresponds to the 95th percentile of observed negative DIV_{WSS} (red-contoured, white regions). The largest $\overline{WSS}$ are localized close to the contact line, although uniform large values are observed all over the portion of the retinal surface in contact with SO. Horizontal bands of large negative values of DIV_{WSS} are observed in the aqueous at the intermediate heights of the inferior region, indicating the presence of an attracting manifold, as also suggested by the field lines of the $\overline{WSS}$ vector. In the case of staphyloma (Fig. 8c,d), large $\overline{WSS}$ are observed at the convex regions at the borders of the posterior bulge, in addition to those close to the contact line. In Fig. 8(a,b), there is a small region with values of $DIV_{WSS} >$ 95th percentile, where streamlines converge, and a critical point of the vector field is localised. Repelling manifolds (black regions) are localized just below the contact line.

In the cerclage case, large values of $\overline{WSS}$ are instead localized at the equatorial portion of the indentation, where the retina is in contact with SO and, similarly to the other cases, close to the contact line. Elongated attracting manifolds develop along the rising menisci, as highlighted by the white regions. Interestingly, similar persistent patterns are observed also for the other investigated motions (Fig. 9). The presence of these WSS patterns at the retinal surface, quantified via the 95th percentile, suggests that fluid dynamics drives an alteration of the biochemical transport with a possible accumulation of pro-inflammatory molecules and cells along elongated attracting manifolds and the potential onset of proliferative processes, in agreement with in-vivo observations. In the saccade, the surface area with $DIV_{WSS} < 1000$ Pa/m is $\approx$50 cm^2 for the emmetropic and staphyloma cases, while increases up to $\approx$120 cm^2 with the cerclage, suggesting a more disordered flow with a different manifold picture, even for a simple movement.

With reference to Fig. 1, the initial-stage PVR depicted by a localized retinal fold is reminiscent of the initial proliferation along regions of intense accumulation such as critical points observed in Fig. 8(a). Multiple starfolds shown in Fig. 1(b) are instead compatible with the topology of the attracting manifolds, regions of preferential accumulation of biochemicals.

We infer that proliferation may occur along these regions with abnormal values of DIV_{WSS}. It is an established concept of biology that gradients of signalling molecules drive the concentration of circulating cells such as monocytes and "tissue sentinels" such as macrophages. The vitreous chamber is no exception and contains cells belonging to the same cellular line, known as hyalocytes (Joshi et al., 2013).

In Fig. 9, we rationalize the smaller values of surface-average WSS in the car braking case (Fig. 4): the SO-phase presents small values of WSS, impacting the whole surface integral. The head rotation, a combination of linear and angular accelerations, presents intermediate values. We can infer that (i) saccadic movements promote more intense dynamics compared to the other everyday movements, and (ii) horizontal linear accelerations appear to have a lower impact on SO displacement. Conversely, gas-tamponade (Rossi et al., 2023) shows large WSS values induced by sloshing.

To highlight the connection between bulk flow, near-wall transport, and possible clinical consequences, 100 synthetic particles are released uniformly in the proximity of the retinal surface every 0.25 s and then tracked during 10 repetitions of the head rotation (25 s). Their final distribution (Fig. 10) shows that particles accumulate at the almost-horizontal annular attracting manifold located in the inferior region, in the vicinity of the uprising water meatus. In the cerclage case, accumulation near the rising menisci confirms the scenario described by manifold theory.

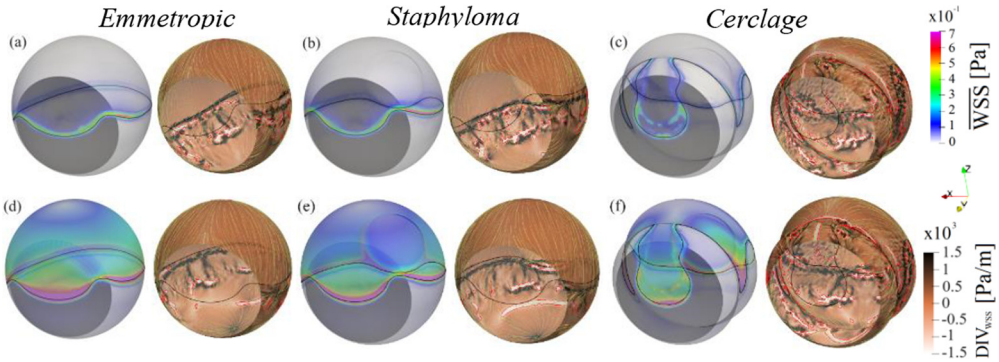

Fig. 9. Same as Fig. 8 in the (a,b,c) car braking and (d,e,f) head rotation cases, for the (a,d) emmetropic, (b,e) staphyloma and (c,f) encirclement cases.

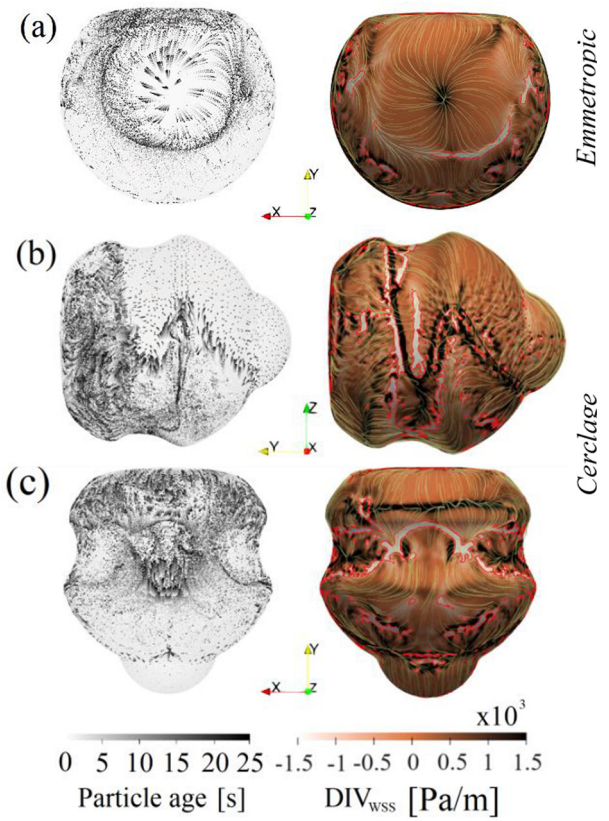

Fig. 10. Distribution of synthetic particles seeded in the neighbourhood of the wall after ten repetitions of the head rotation (on the left); colormap of DIV_{WSS} (on the right), for the (a) emmetropic eye and (b,c) cerclage. The red-contoured, white regions denote the attracting manifolds, defined by the threshold value DIV_{WSS} = 1000 Pa/m. (For interpretation of the references to colour in this figure legend, the reader is referred to the web version of this article.)

6. Discussion and conclusions

Though patients undergoing retinal surgery and vitrectomy with an injection of SO tamponade are instructed to maintain prescribed postures as long as possible, some everyday movements are unavoidable. We numerically analysed a subset of movements developing in the horizontal plane.

We observed common features irrespective of the driving movement and eye geometry that retain suggestive similarities with the clinical presentation of proliferative vitreoretinopathy: (*i*) the highest WSS are found at the contact line, which hardly moves; (*ii*) the highest velocities are attained in the aqueous, at an intermediate "meridional latitude"; (*iii*) in the same regions, we observe horizontally elongated attracting manifolds of the average velocity field. These manifolds depict regions of increased probability of accumulation of cells transported by the near-wall flow, which may cause inflammation and subsequent proliferative processes. A staphyloma induces high shear-stresses also at its convex borders, whilst the application of a cerclage generates high WSS at the indentation and additional vertically elongated attracting manifolds in the posterior uprising menisci, which appear to be exposed to the accumulation of inflammatory cells with the possibly associated proliferation and retinal re-detachment. Interestingly, the apposition of encircling elements is known to alter the incidence and presentation of proliferative vitreoretinopathy (Abu Eleinen et al., 2018).

Our CFD model suffers from some limitations: (*i*) the transport here modelled is passive, thus not accounting for osmotic flows; (*ii*) the interface and contact angle properties are reproduced through a VOF method, known to present reduced accuracy for quantities at the interface, e.g. when quantifying emulsification. Also, we considered a few (idealized) eye geometries, a single eye inclination and a subset of movements occurring in the horizontal plane. Further analyses would assess the relative effect of diverse movements, eye orientations with respect to the vertical direction, and geometries. However, we observed the emergence, in the aqueous region, of similar patterns despite significant modifications of the eye geometry and motion. In perspective, further simulations would help in better defining regions prone to the accumulation of biochemicals, and the pathogenic risk could be assessed through the introduction of indexes related, for instance, to WSS structure (Morbiducci et al., 2020). Similar analyses may be complementary to those of Chan et al. (2011,2014,2015), giving practical information on risk assessment and sloshing relaxation times, the latter of practical interest in surgical follow-up guidelines when prescribing patient positions.

CRediT authorship contribution statement

P.G. Ledda: Conceptualization, Methodology, Software, Formal analysis, Investigation, Visualization, Writing – original draft, Writing – review & editing. **T. Rossi:** Conceptualization, Investigation, Visualization, Writing – review & editing. **M.G. Badas:** Conceptualization, Methodology, Investigation, Writing – review & editing. **G. Querzoli:** Conceptualization, Methodology, Investigation, Visualization, Writing – review & editing, Supervision.

Declaration of Competing Interest

The authors declare that they have no known competing financial interests or personal relationships that could have appeared to influence the work reported in this paper.

Acknowledgements

This work received support through the ISCRA class C projects IsC99_FLUOS and IsCa9_INOC as well as by the University of Cagliari.

Appendix A. Supplementary material

Supplementary data to this article can be found online at https://doi.org/10.1016/j.jbiomech.2023.111914.

References

Abu Eleinen, K.G., Mohalhal, A.A., Ghalwash, D.A., Abdel-Kader, A.A., Ghalwash, A.A., Mohalhal, I.A., Abdullatif, A.M., 2018. Vitrectomy with scleral buckling versus with inferior retinectomy in treating primary rhegmatogenous retinal detachment with PVR and inferior breaks. Eye 32, 1839–1844. https://doi.org/10.1038/s41433-018-0194-0.

Ando, F., Miyake, Y., Oshima, K., Yamanaka, A., 1986. Temporary use of intraocular silicone oil in the treatment of complicated retinal detachment. Graefe's Arch. Clin. Exp. Ophthalmol. 224, 32–33. https://doi.org/10.1007/BF02144129.

Angunawela, R.I., Azarbadegan, A., Aylward, G.W., Eames, I., 2011. Intraocular fluid dynamics and retinal shear stress after vitrectomy and gas tamponade. Invest. Ophthalmol. Vis. Sci. 52, 7046. https://doi.org/10.1167/iovs.10-6872.

Arzani, A., Gambaruto, A.M., Chen, G., Shadden, S.C., 2016. Lagrangian wall shear stress structures and near-wall transport in high-Schmidt-number aneurysmal flows. J. Fluid Mech. 790, 158–172. https://doi.org/10.1017/jfm.2016.6.

Arzani, A., Gambaruto, A.M., Chen, G., Shadden, S.C., 2017. Wall shear stress exposure time: a Lagrangian measure of near-wall stagnation and concentration in cardiovascular flows. Biomech. Model. Mechanobiol. 16, 787–803. https://doi.org/10.1007/s10237-016-0853-7.

Arzani, A., Shadden, S.C., 2016. Characterizations and correlations of wall shear stress in aneurysmal flow. J. Biomech. Eng. 138, 014503 https://doi.org/10.1115/1.4032056.

Arzani, A., Shadden, S.C., 2018. Wall shear stress fixed points in cardiovascular fluid mechanics. J. Biomech. 73, 145–152.

Barbosa, G.C.S., Silva, A.G.D., Daher Gonçalves Monteiro Dos Reis, G., Bermudes, F.H., Lemos, C.M.B., Garcia, R., Mazzeo, T.J.M.M., Machado, C.G., Gomes, A.M.V., 2022. Large inferior retinectomies for proliferative vitreoretinopathy in silicone oil-filled eyes. Int. J. Retin. Vitr. 8, 73. https://doi.org/10.1186/s40942-022-00420-1.

Bonnet, M., Santamaria, E., Mouche, J., 1987. Intraoperative use of pure perfluoropropane gas in the management of proliferative vitreoretinopathy. Graefe's Arch. Clin. Exp. Ophthalmol. 225, 299–302. https://doi.org/10.1007/BF02150153.

Chan, Y.K., Ng, C.O., Knox, P.C., Garvey, M.J., Williams, R.L., Wong, D., 2011. Emulsification of silicone oil and eye movements. Invest. Ophthalmol. Vis. Sci. 52, 9721. https://doi.org/10.1167/iovs.11-8586.

Chan, Y.K., Williams, R.L., Wong, D., 2014. Flow behavior of heavy silicone oil during eye movements. Invest. Ophthalmol. Vis. Sci. 55, 8453–8457. https://doi.org/10.1167/iovs.14-15439.

Chan, Y.K., Sy, K.H.S., Wong, C.Y., Man, P.K., Wong, D., Shum, H.C., 2015. In vitro modeling of emulsification of silicone oil as intraocular tamponade using microengineered eye-on-a-chip. Invest. Ophthalmol. Vis. Sci. 56, 3314. https://doi.org/10.1167/iovs.15-16728.

Chaudhary, R., Scott, R.A.H., Wallace, G., Berry, M., Logan, A., Blanch, R.J., 2020. Inflammatory and fibrogenic factors in proliferative vitreoretinopathy development. Trans. Vis. Sci. Tech. 9, 23. https://doi.org/10.1167/tvst.9.3.23.

De Nisco, G., Tasso, P., Calò, K., Mazzi, V., Gallo, D., Condemi, F., Farzaneh, S., Avril, S., Morbiducci, U., 2020. Deciphering ascending thoracic aortic aneurysm hemodynamics in relation to biomechanical properties. Med. Eng. Phys. 82, 119–129.

De Silva, D.J., 2005. An experimental study on the effect of encircling band procedure on silicone oil emulsification. Brit. J. Ophthalmol. 89, 1348–1350. https://doi.org/10.1136/bjo.2004.063768.

Fawcett, I.M., Williams, R.L., Wong, D., 1994. Contact angles of substances used for internal tamponade in retinal detachment surgery. Graefe's Arch. Clin. Exp. Ophthalmol. 232, 438–444. https://doi.org/10.1007/BF00186587.

Gambaruto, A.M., João, A.J., 2012. Flow structures in cerebral aneurysms. Comput. Fluids 65, 56–65. https://doi.org/10.1016/j.compfluid.2012.02.020.

Hostovsky, A., Mandelcorn, M.S., Mandelcorn, E.D., 2020. Orbital magnetic resonance imaging demonstrates better contact between the gas and anterior inferior retina in side versus face-down position. Ophthalmol. Retina 4, 911–918. https://doi.org/10.1016/j.oret.2020.03.029.

Isakova, K., Pralits, J.O., Romano, M.R., Beenakker, J.-W.-M., Shamonin, D.P., Repetto, R., 2017. Equilibrium shape of the aqueous humor-vitreous substitute interface in vitrectomized eyes. MAIO 1, 31–46. https://doi.org/10.35119/maio.v1i3.36.

Joshi, M., Agrawal, S., Christoforidis, J.B., 2013. Inflammatory mechanisms of idiopathic epiretinal membrane formation. Med. Inflam. 2013, 1–6. https://doi.org/10.1155/2013/192582.

Kleinberg, T.T., Tzekov, R.T., Stein, L., Ravi, N., Kaushal, S., 2011. Vitreous substitutes: a comprehensive review. Surv. Ophthalmol. 56, 300–323. https://doi.org/10.1016/j.survophthal.2010.09.001.

Ledda, P.G., Badas, M.G., Matta, G., Querzoli, G., 2023. Flow dynamics in a model of a dilated thoracic aorta prior to and following prosthetic replacement. Theor. Comput. Fluid Dyn. https://doi.org/10.1007/s00162-023-00651-4.

Lewis, G.P., Charteris, D.G., Sethi, C.S., Leitner, W.P., Linberg, K.A., Fisher, S.K., 2002. The Ability of Rapid Retinal Reattachment to Stop or Reverse the Cellular and Molecular Events Initiated by Detachment 43.

Mazzi, V., Gallo, D., Calò, K., Najafi, M., Khan, M.O., De Nisco, G., Steinman, D.A., Morbiducci, U., 2020. A Eulerian method to analyze wall shear stress fixed points and manifolds in cardiovascular flows. Biomech. Model. Mechanobiol. 19, 1403–1423.

Mazzi, V., Morbiducci, U., Calò, K., De Nisco, G., Lodi Rizzini, M., Torta, E., Caridi, G.C. A., Chiastra, C., Gallo, D., 2021. Wall shear stress topological skeleton analysis in cardiovascular flows: methods and applications. Mathematics 9, 720.

Morbiducci, U., Mazzi, V., Domanin, M., De Nisco, G., Vergara, C., Steinman, D.A., Gallo, D., 2020. Wall shear stress topological skeleton independently predicts long-term restenosis after carotid bifurcation endarterectomy. Ann. Biomed. Eng. 48, 2936–2949.

Romano, M.R., Ferrara, M., Nepita, I., D'Amato Tothova, J., Giacometti Schieroni, A., Reami, D., Mendichi, R., Liggieri, L., Repetto, R., 2021. Biocompatibility of intraocular liquid tamponade agents: an update. Eye 35, 2699–2713. https://doi.org/10.1038/s41433-021-01596-w.

Rossi, T., Querzoli, G., Badas, M.G., Angius, F., Telani, S., Ripandelli, G., 2021. Computational fluid dynamics of intraocular silicone oil tamponade. Trans. Vis. Sci. Tech. 10, 22. https://doi.org/10.1167/tvst.10.8.22.

Rossi, T., Querzoli, G., Badas, M.G., Angius, F., Ripandelli, G., 2022. Silicone oil tamponade-retina contact in highly myopic eyes with and without encircling bands: a computational fluid dynamics study. Trans. Vis. Sci. Tech. 11, 1. https://doi.org/10.1167/tvst.11.6.1.

Rossi, T., Badas, M.G., Angius, F., Querzoli, G., 2023. Do daily activities affect gas tamponade-retina contact after pars plana vitrectomy?: A computational fluid dynamics study. Retina 43, 955–963. https://doi.org/10.1097/IAE.0000000000003750.

Stocchino, A., Repetto, R., Siggers, J.H., 2010. Mixing processes in the vitreous chamber induced by eye rotations. Phys. Med. Biol. 55, 453–467. https://doi.org/10.1088/0031-9155/55/2/008.

Wang, R., Snead, M., Alexander, P., Ian Wilson, D., 2021. Assessing bulk emulsification at the silicone oil – saline solution interface in a 3D model of the eye. Acta Ophthalmol. 99 https://doi.org/10.1111/aos.14539.

Wei, Y., Wu, G., Xu, K., Wang, J., Zu, Z., Wang, R., 2016. The outcomes of scleral buckling versus re-vitrectomy for the treatment of recurrent inferior retinal detachment in silicone oil tamponade eyes. Acta Ophthalmol. 94, e624–e628. https://doi.org/10.1111/aos.13037.

Weller, H.G., Tabor, G., Jasak, H., Fureby, C., 1998. A tensorial approach to computational continuum mechanics using object-oriented techniques. Comput. Phys. 12, 620. https://doi.org/10.1063/1.168744.